

# Absolute linear-angular synchronous positioning at the microscale based on a metasurface array reflector

Wanghang Gu (谷望航)\*, Junchen Liu (刘俊辰), Xueyan Lin (林雪妍), Xinghua Qu (曲兴华), and Fumin Zhang (张福民)\*\*  
State Key Laboratory of Precision Measurement Technology and Instruments, Tianjin University, Tianjin 300072, China

\*Corresponding author: [guwanghang@163.com](mailto:guwanghang@163.com)

\*\*Corresponding author: [zhangfumin@tju.edu.cn](mailto:zhangfumin@tju.edu.cn)

Received October 15, 2024 | Accepted December 18, 2024 | Posted Online May 16, 2025

In this research, we report a two-dimensional pose measurement scheme based on a metasurface array reflector, which enables absolute tracking of both linear and angular positions. The metasurface array reflector, utilizing the tailored optical field characteristics of a plasmonic absorption structure, simultaneously responds to linear and angular displacements within the illuminated optical field range and provides a characteristic absolute code to the receiving end. This code can be used to map the target's linear and angular position. By matching it with a pre-established template network, it is possible to track the target's absolute position. Under  $\mu\text{m}$ -level linear displacements and  $\mu\text{rad}$ -level angular displacements, we achieved precise two-dimensional linear and angular tracking and positioning based on this device.

**Keywords:** metasurface; precision positioning; optical measurement; precision measurement.

**DOI:** [10.3788/COL202523.061201](https://doi.org/10.3788/COL202523.061201)

## 1. Introduction

The multi-degree-of-freedom (MDOF) synchronous precision positioning technology at the microscale plays a crucial role such as robotic control, lithographic alignment, complex motion tracking, and 3D perception<sup>[1-4]</sup>. The MDOFs include linear quantities in three directions ( $x$ ,  $y$ ,  $z$ ) as well as angular quantities around three axes (roll, yaw, pitch). When measuring linear and angular quantities of a single degree of freedom (DOF), the methods represented by laser interferometry and self-collimation have been quite mature. However, in practical engineering applications, there are often scenarios where MDOFs need to be measured simultaneously, yet the approach of sequential measurements is still commonly employed. Therefore, many researchers have proposed a variety of MDOF measurement schemes, including combinations of linear quantities across different dimensions<sup>[5-7]</sup> or combinations of linear and angular quantities<sup>[8,9]</sup>. Among these, the linear-angular synchronous measurement is particularly challenging because angular data are more difficult to acquire, often necessitating the construction of more complex systems or the introduction of more precise devices.

Typically, linear and angular quantities can be acquired by placing sensing devices such as prisms or gratings on the target side<sup>[10-12]</sup>. These solutions often rely on interferometry setups, converting geometric displacements in each DOF into axial optical path differences for subsequent analysis, while also requiring multiple detectors to jointly receive information across different

DOFs. Both of these factors lead to an increase in system complexity, making it difficult to meet the current demands for lightweight and miniaturized measurement systems. On the other hand, in practical engineering applications, the traceability of a target's position is often required, which necessitates absolute geometric measurements<sup>[13-16]</sup> and positioning techniques<sup>[17,18]</sup>. However, traditional devices typically perform relative measurements, making it difficult to achieve absolute encoding. Therefore, developing a novel sensing device and measurement scheme that enables simultaneous absolute positioning of both linear displacement and angular measurements with a simplified system holds significant importance.

In recent years, nanophotonics has enabled beam manipulation at the subwavelength scale, pushing light control beyond the diffraction limit and creating new possibilities for precision measurements. Metasurfaces, as two-dimensional (2D) metamaterials with subwavelength structures, can manipulate electromagnetic beams by controlling the wavefront phase, amplitude, and polarization<sup>[19-21]</sup>. Previous studies have demonstrated that the manipulation of incident light fields by metasurfaces can be utilized for one-dimensional (1D) and 2D geometric measurements<sup>[22-24]</sup>, achieving promising results. Building upon this, some researchers have proposed a metasurface-based array with high customization to achieve specific filtering functions, which has been widely applied in molecular detection, pattern recognition, and spectral analysis<sup>[25-28]</sup>. The unique feature of this approach lies in the ability to discretely manipulate different wavelength components of the incident

light through the customized design of each subunit, thereby enabling the analysis of spectral information. Similarly, due to its special manipulation capabilities within the 2D plane, this device can respond to the relative position of the incident light, thus acting as a sensor to track the target position. Moreover, as it can provide a visual output of the incident light information, it possesses high information encoding capacity, enabling a one-to-one correspondence between the target quantities and the visualized information, thereby facilitating absolute encoding. Compared to using devices like gratings as reflectors, the metasurface array, with its unique light field manipulation properties and wavelength-angle selectivity, can further map spectral information to light intensity, enhancing the response to position changes while providing a visualizable spectral output, making absolute position encoding possible. Due to the arrayed integration design, it can achieve higher sensitivity at a lower precision manufacturing cost, which is advantageous in compact optical reflectors.

In this work, we propose a scheme for simultaneous measurement of angular and linear displacements. This scheme is based on a metasurface array reflector with customized light-field manipulation capabilities. The subunits of the metasurface are designed using plasmonic absorber structures, offering wavelength selectivity, which allows the separation of different wavelength components of the incident light at varying angles. When a broadband laser source illuminates the metasurface, it generates a characteristic spot array corresponding to each subunit within the device area. This spot array, serving as a distinctive pattern, responds differently to displacement and angular variations. After calibration, these features can be used to track the linear-angular absolute position. We developed a measurement scheme based on this device and built a system that can simultaneously perform microscale 2-DOF absolute measurements of linear and angular displacements using a single detector.

## 2. Principle

As shown in Fig. 1(a), a schematic of the proposed metasurface array for providing absolute feedback of two DOFs in linear and angular positions is provided. The overall scheme is as follows: a multi-wavelength laser source, coupled by a collimator lens (COL), illuminates the metasurface array, where the absolute linear-angular position is encoded in the visualized absolute code formed by the reflection of the incident light on the device. Absolute code serves as a marker for tracking the position of the target and is received and processed by a charge-coupled device (CCD) camera coupled with a telecentric lens. When the metasurface undergoes 2-DOF displacement, including in-plane displacement ( $x$ ) and angular rotation ( $\tau$ ), the pattern changes. The mechanism of this change is related to the metasurface design.

As illustrated in Fig. 1(b), the specific formation process of absolute code is explained in detail. The metasurface is a sub-wavelength device with a periodic arrangement of nanoscale

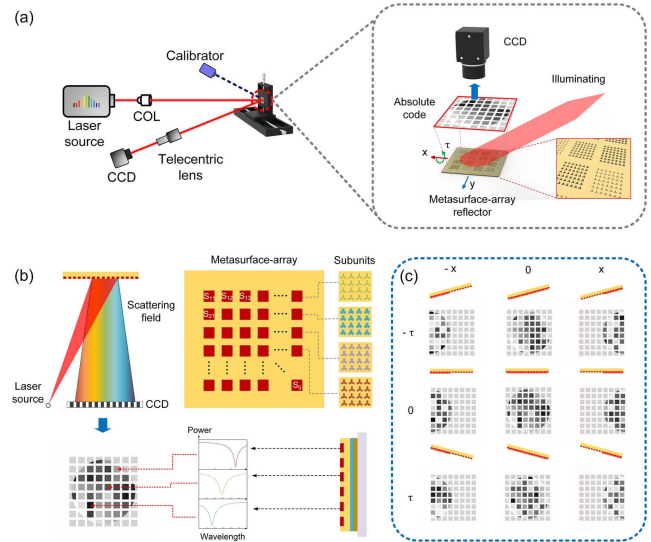


**Fig. 1.** Principle of absolute linear-angular positioning. (a) Schematic diagram of the overall scheme. The inset shows the absolute code that reflects the linear-angular displacements. (b) Principle of absolute code formation. (c) The mapping relationship between  $x$ - $\tau$  position and absolute code.

patterns on its surface. When a multi-wavelength source is incident upon the metasurface, the subwavelength microstructure causes different wavelength components of the incident light to scatter at different angles, resulting in a wavelength-dependent angular distribution of the scattered field. The metasurface array is divided into distinct regions (subunits) in a 2D plane, with each subunit comprising a rectangular arrangement of structural atoms in specific configurations. The optical field manipulation characteristics of the metasurface are determined by the structure of these cells; thus, each subunit corresponds to a unique absorption spectrum.

Figure 2 presents the design of the metasurface unit cells. The metasurface unit cells adopt a series of rotationally symmetric structures ( $C_n$ ) with a specific 3-rotational-arm slot structure ( $C_3$ ), as shown in Fig. 2(a). The slot width  $w$  is set as the characteristic size to alter the unit cell's geometric structure, modulating the metasurface's performance. A total of 19 different unit cell structures are designed, with the  $w$  values ranging from  $w_0$  to  $w_{18}$ . The arrays of unit cells with different  $w$  values form distinct subunits, which are distributed in different regions of the metasurface array. Figure 2(b) specifically illustrates the design of the unit cells. The unit cell's duty cycle is set according to the half-wavelength requirement, with the array periodic length  $a = 690$  nm, the  $C_3$  rotational arm length  $l = 250$  nm, and the characteristic dimension  $w_0$ - $w_{18}$  ranging from 180 to 280 nm.

Figure 2(b) also displays a side view of the unit cell, revealing the material composition of the metasurface. The metasurface is designed based on a plasmonic absorber structure, employing a metal-insulator-metal (MIM) architecture, which is a typical configuration of a plasmonic metasurface. The structure utilizes the surface plasmon resonance (SPR) effect to achieve highly controllable optical properties. Functionally, this structure

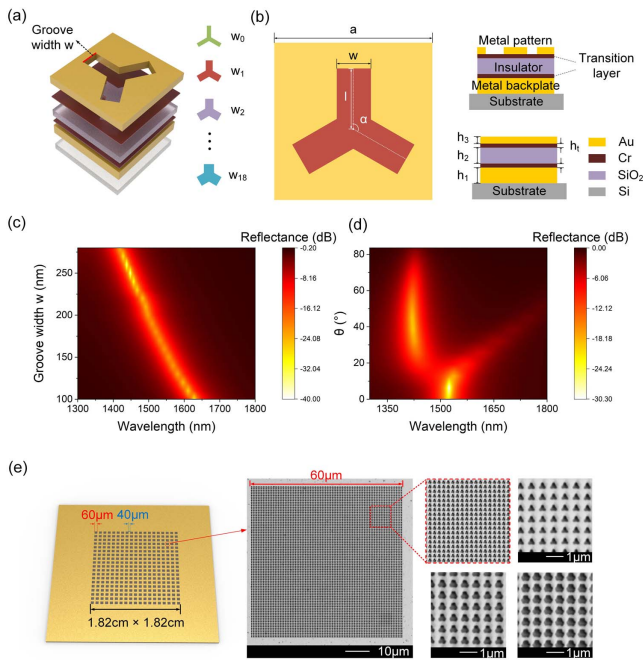


**Fig. 2.** Design and fabrication of the metasurface array device. (a) Schematic of the unit cell. (b) Planar and sectional design of the unit cell. (c) Graph depicting the relationship among  $w$ , wavelength, and reflectance. (d) Graph depicting the relationship among incident angle  $\theta$ , wavelength, and absorption rate. (e) SEM characterization of different subunits.

consists of several layers: the metal pattern, the insulator, and the metal backplane. A transition metal layer is introduced between the metal and non-metal layers to guide material deposition. The thicknesses of the layers are as follows: the backplane layer  $h_1 = 200$  nm, the insulator layer  $h_2 = 145$  nm, the structural layer  $h_3 = 55$  nm, and the chromium transition layer  $h_t = 5$  nm.

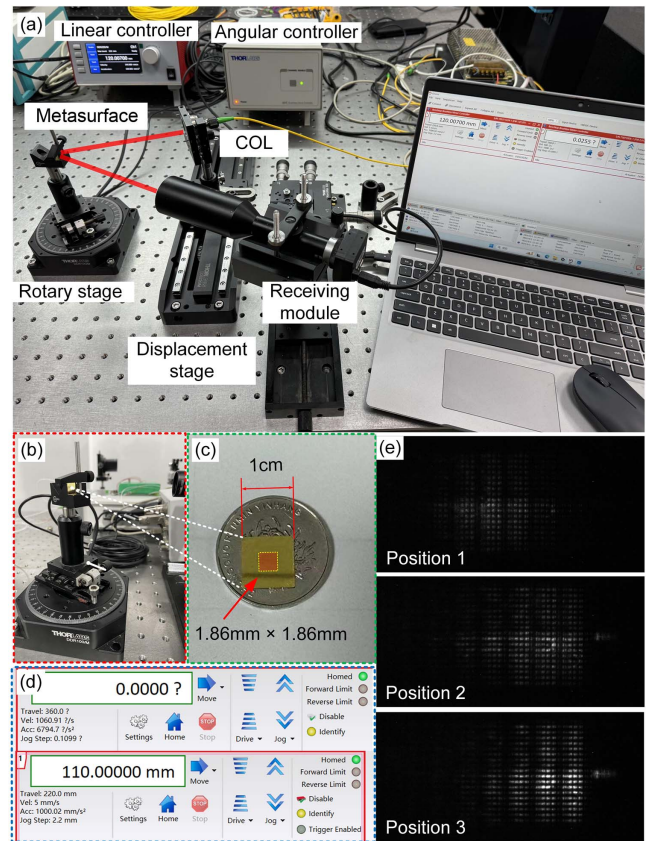
The value of  $w$  determines the absorption performance of the corresponding unit cell, which means that the peak of the absorption spectrum at different values of  $w$  corresponds to different wavelengths. Figures 2(c) and 2(d) show the finite difference-time domain (FDTD) simulation results of the  $C_3$  unit cells. Figure 2(c) illustrates the reflection spectra for different values of  $w$ . It can be observed that different values of  $w$  correspond to different wavelengths with varying reflectivities, reflecting the wavelength-selective absorption characteristics of the  $C_3$  structure. Moreover, when the value of  $w$  ranges between 180 and 280 nm, the absorption peaks lie within the 1410 to 1620 nm band. Figure 2(d) presents the relationship among the incident angle  $\theta$ , wavelength, and absorption rate. Figure 2(e) demonstrates the overall design of the metasurface array device and its scanning electron microscope (SEM) characterization. The size of a single subunit is  $60\ \mu\text{m} \times 60\ \mu\text{m}$ , and the spacing between adjacent subunits is  $40\ \mu\text{m}$ . We believe that the key to the functionality of the metasurface lies in the structural differences of unit cells within each subunit. Therefore, the fabrication precision of the characteristic dimension  $w$  is critical. The SEM characterization displays the overall morphology of the subunit and the processing results of unit cells with different

values of  $w$ . The results indicate that the fabrication process successfully realizes the  $C_3$  structure and allows for clear resolution of the characteristic size.

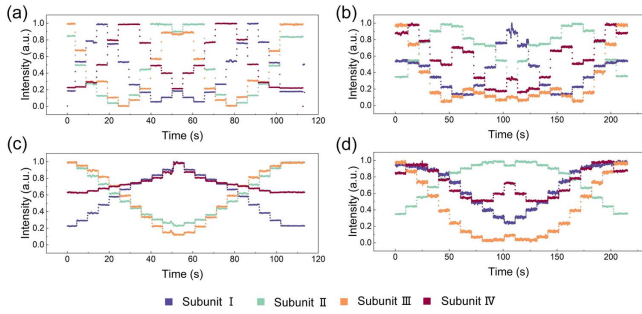
### 3. Experimental Setup

Figure 3(a) shows the experimental setup we built for the linear-angular synchronous positioning. A coupling lens is connected to the multi-wavelength laser source via a single-mode fiber. After being reflected by the metasurface, the laser beam is received by the receiving module composed of a CCD and a telecentric lens.

The metasurface is mounted on a combined mechanism that includes both a sliding module and a precision rotary stage, as shown in Fig. 3(b). Additionally, the COL is mounted on a precision displacement stage. This setup allows for two-DOF position adjustments (linear displacement and angular rotation) between the laser spot and the metasurface by synchronously controlling the rotation and translation stages. Both of them are controlled by servo controllers. Figure 3(d) shows the upper-level control interface for the two-DOF synchronous control of linear displacement and angular rotation.



**Fig. 3.** Experimental setup. (a) Photograph of the experimental setup. (b) Clamping setup of the metasurface array reflector. (c) Photograph of the metasurface array reflector. (d) Interface of the two-DOF synchronous control system. (e) Images captured by the CCD at three distinct linear-angular positions.



**Fig. 4.** Sensitivity characterization of different subunits to linear and angular responses when (a)  $\Delta x = 50 \mu\text{m}$ , (b)  $\Delta \tau = 170 \mu\text{rad}$ , (c)  $\Delta x = 10 \mu\text{m}$ , and (d)  $\Delta \tau = 85 \mu\text{rad}$ .

As shown in Fig. 3(c), the actual metasurface array reflector we fabricated has an overall square shape with a dimension of  $1 \text{ cm} \times 1 \text{ cm}$ . The red area in the image indicates the functional patterned region, with an area of  $1.86 \text{ mm} \times 1.86 \text{ mm}$ . It can be observed that our designed device has a relatively small working size, which allows for easy deployment in various complex application scenarios. Figure 3(e) shows the images captured by the CCD under three different linear-angular 2D target states. As can be seen, due to the different absorption characteristics of the subunits, the scattering pattern presents a series of light and dark spots, and the grayscale features respond to changes in the linear-angular pose. Four distinct subunits are selected from the image and labeled as I–IV, respectively. To characterize the sensitivity of the absolute code to displacement and rotation, the step size of the rotary and displacement stages were set to  $\Delta x = 50 \mu\text{m}$ ,  $\Delta x = 0 \mu\text{m}$ ,  $\Delta \tau = 170 \mu\text{rad}$ , and  $\Delta \tau = 85 \mu\text{rad}$ . The brightness variations of subunits I–IV were recorded under these conditions, and the results are shown in Fig. 4.

From the results, it can be observed that different subunits exhibit varying absorption intensities at the same moment, and the trends of change differ with respect to displacement and angular variations. At the specified step sizes, clear step signals can be observed, demonstrating the system's robust response characteristics to incremental changes in linear and angular position states. Therefore, the absolute code generated from the intensity differences between the subunits can simultaneously encode both linear displacement and angular rotation, establishing a one-to-one mapping with the linear-angular position states.

#### 4. Linear-Angular Position Encoding

We identified four target positions, as shown in Fig. 5(a), labeled as  $P_0$ – $P_3$ .  $P_0$  represents the initial position,  $P_1$  is the position after one step along the linear  $x$ -axis,  $P_2$  is the position after one step of angular deflection along the  $\tau$ -axis, and  $P_3$  is the position after a simultaneous single-step movement along both the linear and angular axes.

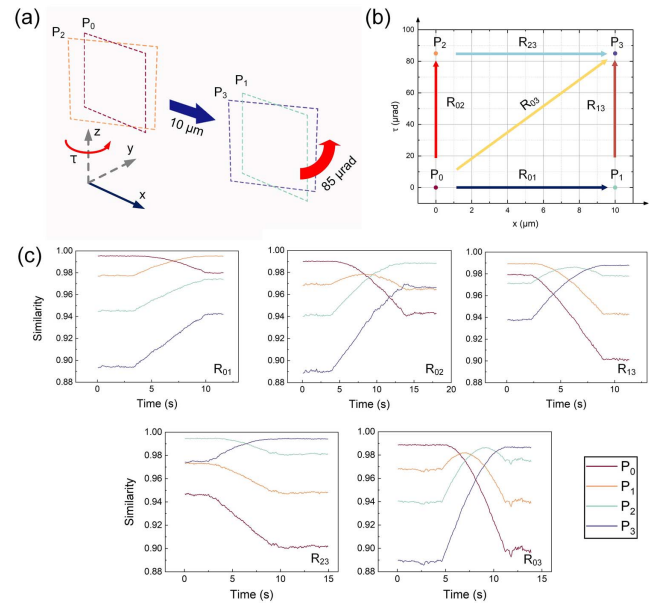


**Fig. 5.** Linear-angular single-step operation experiment. (a) Schematic of the four positions. (b) Schematic of the movement paths. (c) Similarity variation trend with the four positions as templates.

After determining the four positions, we further established five movement routes between these points, as shown in Fig. 5(b). The route from  $P_0$  to  $P_1$  is labeled as  $R_{01}$ , and the route from  $P_0$  to  $P_2$  is labeled as  $R_{02}$ , and so on. First, we collected images at the four positions  $P_0$ – $P_3$  as reference position templates. Then, during the movement of the rotation and displacement stages along the respective routes, we continuously collected images in real time. Finally, the captured images were compared with the four reference positions to compute their similarity, as shown in Fig. 5(c).

Using route  $R_{01}$  as an example, the initial state is at  $P_0$ , where the similarity to  $P_0$  is the highest, and the similarity to  $P_3$  is the lowest. As the position moves toward  $P_1$ , the similarity to  $P_1$  gradually reaches its maximum. At both the beginning and the end of the process, the similarity of the four points does not overlap, allowing for clear differentiation. By quantifying the similarity values, we can select the best matching template with the highest similarity to determine the position of the target. Overall, in all four single-DOF movement routes, the best matching templates for both the initial and final states correspond to the actual positions. In the case of simultaneous linear and angular movement along route  $R_{03}$ , the highest similarity at both the initial and final states also matches the position, proving that the 2-DOF position can be accurately tracked using this scheme. When implementing 2-DOF position detection using a single device, it is essential to consider the crosstalk between different dimensions in the detection process. For instance, during the purely linear movement of  $R_{01}$ , the similarity to points  $P_2$  and  $P_3$ , which involve angular displacement, remains consistently low and stable throughout the process, not interfering with the selection of the best match. Similarly, the purely linear movement along  $R_{23}$  exhibits a stable, linear similarity change

with each template throughout the process, akin to  $R_{01}$ . However, in the purely angular movement along  $R_{02}$ , the similarity to point  $P_1$ , which involves linear displacement, and the similarity along  $R_{13}$  with point  $P_2$  exhibit non-linear changes and show more pronounced fluctuations compared to purely linear movement. This suggests that determining angular positions may be prone to interference from linear displacement. This is typically due to the difficulty in maintaining coaxiality during angular rotation; that is, there is a certain micro-displacement during the angle change.

### 5. Linear-Angular Tracking and Positioning

Based on the previous experimental results, it can be determined that when the pose state changes, by matching it with the pre-acquired templates, the absolute code can serve as a “label” to track the linear-angular 2D position of the target. Therefore, we further demonstrated continuous 2D position tracking.

First, a sufficient number of templates must be collected for the two DOFs. As shown in Fig. 6(a), the target operates along the  $x$ -axis and  $\tau$ -axis. First, we establish a coordinate system with these two axes. A network is constructed with displacement steps of  $1\ \mu\text{m}$  along the  $x$ -axis and rotational steps of  $8.5\ \mu\text{rad}$  along the  $\tau$ -axis, where each node represents a specific 2D position. In the red-marked region, templates are collected at each

node, with the  $x$ -axis ranging from 0 to  $30\ \mu\text{m}$  and the  $\tau$ -axis ranging from 0 to  $467.5\ \mu\text{rad}$ . Given the step sizes on each axis, it can be calculated that there are 1736 nodes within the constructed template network (TN), including the boundaries, meaning a total of 1736 templates are collected.

As described in Fig. 1(a), a higher-level calibration tool is used for correction during template collection. For displacement and angular templates, we, respectively, use a laser interferometer and a laser autocollimator for synchronized measurements to ensure that the template positions correspond to the true values. After template collection, at the position  $x = 5\ \mu\text{m}$ , we run the angle  $\tau$  in 5 steps with a step size of  $85\ \mu\text{rad}$ , from  $\tau = 0\ \mu\text{rad}$  to  $\tau = 425\ \mu\text{rad}$ . This route is denoted as  $L_1$ . Next, the displacement axis moves instantaneously to  $x = 15\ \mu\text{m}$ , and the rotation axis again moves from  $\tau = 0\ \mu\text{rad}$  to  $\tau = 425\ \mu\text{rad}$ , denoted as  $L_2$ . Finally, the displacement axis moves to  $x = 25\ \mu\text{m}$ , and the rotation axis follows the same process, which is denoted as  $L_3$ .  $L_1$ ,  $L_2$ , and  $L_3$  form a continuous sequence with no time intervals in between.

As shown in Fig. 6(b), all images collected throughout the process are matched against all templates in the TN. Since each template in the TN corresponds to a unique 2D pose, the target pose can be identified by matching the image to the template number. Figure 6(b) also shows the numbering scheme for the 1736 templates in the TN. The 31 distinct  $x$  positions are grouped, with each  $x$  position containing 56 corresponding  $\tau$  positions. Starting from  $x = 0\ \mu\text{m}$ , the templates from  $\tau = 0\ \mu\text{rad}$  to  $\tau = 467.5\ \mu\text{rad}$  are labeled No. 1 to No. 56. The subsequent 56 templates for  $x = 1\ \mu\text{m}$  are labeled No. 57 to No. 112, and so on, continuing up to  $x = 30\ \mu\text{m}$  with templates numbered from No. 1681 to No. 1736.

When collecting the TN, due to calibration, the encoder values from the rotation stage and displacement stage can be considered as reference values. Since the templates are numbered based on displacement grouping, during angular stepping changes, the matched template numbers exhibit small step-like changes. Conversely, during displacement stepping changes, the template numbers exhibit large step-like changes. Therefore, as the combined mechanism operates along the  $L_1-L_3$  paths, the template numbers corresponding to the angle-displacement reference values are shown in Fig. 6(c). The three displacement states of  $L_1-L_3$  correspond to three large steps, while the internal angular changes within each path correspond to smaller steps. In the actual operation process, the template numbers that best match the images collected at each time are shown in Fig. 6(d). The results in Figs. 6(c) and 6(d) represent a comparison between reference values and measured values.

By comparing the results from Figs. 6(c) and 6(d) on a macro level, we observe that, for most of the time, the best-matched templates from the tracking system align well with the reference values. In Fig. 6(d), the purple sections correspond to  $L_1$ , the green sections correspond to  $L_2$ , and the orange sections correspond to  $L_3$ . The magnified views of these three segments and the comparison with the reference values are shown in Figs. 6(e)-6(g), respectively. From Fig. 6(d), it is clear that the matching results between the three segments are distinctly

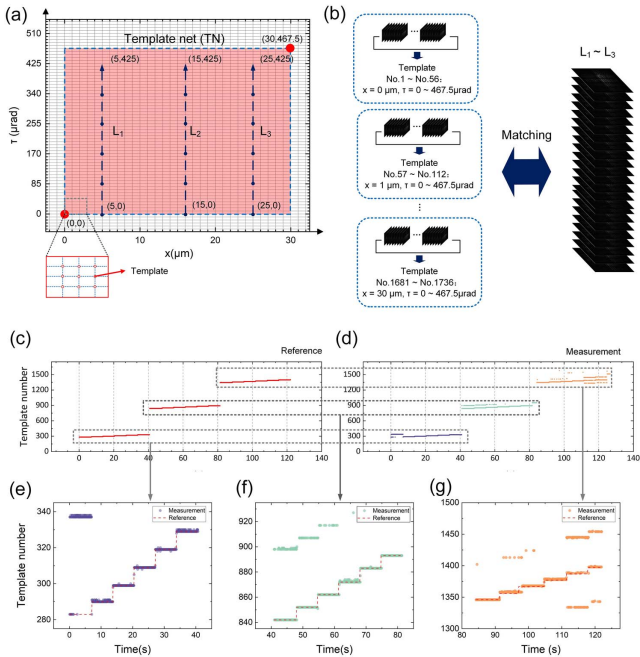


**Fig. 6.** 2D position Tracking. (a) Establishment of the TN. (b) Template naming convention and schematic for pose absolute code matching. (c) Reference values for 2D position template numbers. (d) Matching results between the measured position and the template. (e)-(g) Comparison of reference template numbers and actual template numbers obtained from matching under three routes (e)  $L_1$ , (f)  $L_2$ , and (g)  $L_3$ .

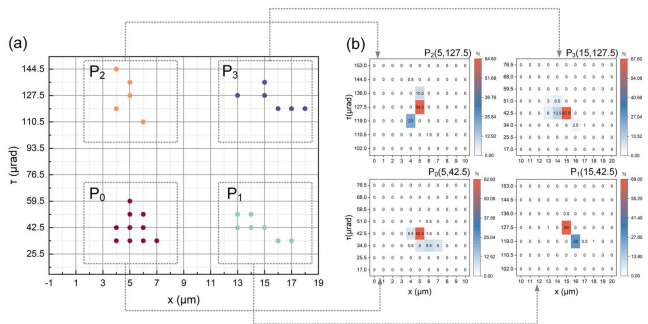


Fig. 7. 2D absolute positioning. (a) Overall positioning point distribution results. (b) Tracking accuracy of each position point.

separated, indicating that the linear displacement changes are clearly distinguished. As shown in Fig. 6(e), at the first step of  $L_1$ , there is an average difference of 54 in the template numbers between the measured values and the reference values, indicating a significant displacement deviation. However, in the subsequent steps, the deviation remains in the single digits, demonstrating that the best-matched templates are all within the same group, with only angular deviations present. In contrast, during  $L_2$  and  $L_3$ , displacement deviations occur more frequently, indicating a higher incidence of mismatch between the measured and reference values. This phenomenon indicates that the position state determined by the best-matched template experiences jitter. This could be due to slight vibrations in the mechanical system itself or surrounding environmental activities. On the other hand, it may also result from the relatively high similarity between adjacent nodes in the TN, leading to errors in template matching.

We set the positional states of the combination mechanism at four positions:  $P_0$  ( $x = 5 \mu\text{m}$ ,  $\tau = 42.5 \mu\text{rad}$ ),  $P_1$  ( $x = 15 \mu\text{m}$ ,  $\tau = 42.5 \mu\text{rad}$ ),  $P_2$  ( $x = 5 \mu\text{m}$ ,  $\tau = 127.5 \mu\text{rad}$ ), and  $P_3$  ( $x = 15 \mu\text{m}$ ,  $\tau = 127.5 \mu\text{rad}$ ). At each position, the system remained stationary for 10 s, with the CCD capturing images at a frame rate of 15 frame/s (fps). Consequently, we obtained 150 images at each position. All images were matched against the TN to track the 2D position, and the overall distribution of the position data is shown in Fig. 7(a). Figure 7(b) shows the distribution of data points obtained by tracking at four positions. It can be seen that the rate of correct positioning of all points is above 60%, the  $\tau$  deviation is within  $\pm 17 \mu\text{rad}$ , and the  $x$  deviation is within  $\pm 2 \mu\text{m}$ . Therefore, the proposed scheme can well achieve 2D absolute position tracking in the two DOFs of  $x - \tau$ . In general, the metasurface array reflector can respond to linear displacement as low as  $1 \mu\text{m}$  and angular displacement as low as  $8.5 \mu\text{rad}$ , and it can achieve good measurement results at this scale.

## 6. Conclusion

We proposed a linear-angular synchronous positioning scheme based on a metasurface array reflector. The proposed metasurface device can respond sensitively and simultaneously to

displacement and angular changes. Through the metasurface array, we can construct a patterned code that can simultaneously map the position on displacement and rotary axes. By establishing a line-angle two-axis TN, this visual absolute code can track the absolute 2D position on linear and angular axes of the target. Since the device has an extremely small working volume, it can be easily applied to various complex applications as a sensor that can respond to complex pose changes.

## Acknowledgements

This work was supported by the National Natural Science Foundation of China (No. 52375546).

## References

1. Y. Li, J. Wu, P. Yang, *et al.*, "Multi-degree-of-freedom robots powered and controlled by microwaves," *Adv. Sci.* **9**, 2203305 (2022).
2. Y. Tang, J. Liu, Y. Yang, *et al.*, "Large range nano alignment for proximity lithography using complex grating," *Opt. Laser Technol.* **112**, 101 (2019).
3. F. Xu, Y. Zhao, L. Ni, *et al.*, "Two-dimensional Hanning self-convolution window for enhancing Moiré fringe alignment in lithography," *Mech. Syst. Signal Process.* **208**, 111052 (2024).
4. L. Zhang, H. Zhan, X. Liu, *et al.*, "A planar compound eye based microsystem for high precision 3D perception," *Photonix* **5**, 21 (2024).
5. K. Zhu, B. Guo, Y. Lu, *et al.*, "Single-spot two-dimensional displacement measurement based on self-mixing interferometry," *Optica* **4**, 729 (2017).
6. H.-L. Hsieh and P.-C. Kuo, "Heterodyne speckle interferometry for measurement of two-dimensional displacement," *Opt. Express* **28**, 724 (2020).
7. Q.-Y. Xin, Y.-C. Pei, B. Wang, *et al.*, "Digital synchronous measurement method for two-dimensional in-plane displacement using check-code," *Measurement* **225**, 114047 (2024).
8. Y. Shimizu, H. Matsukuma, and W. Gao, "Optical sensors for multi-axis angle and displacement measurement using grating reflectors," *Sensors* **19**, 5289 (2019).
9. M. Zhang, H. Yang, Q. Niu, *et al.*, "Combined displacement and angle sensor with ultra-high compactness based on self-imaging effect of optical micro-gratings," *Sensors* **24**, 908 (2024).
10. J. Zhu, G. Wang, S. Wang, *et al.*, "A reflective-type heterodyne grating interferometer for three-degree-of-freedom subnanometer measurement," *IEEE Trans. Instrum. Meas.* **71**, 1 (2022).
11. S. Zhou, V. Le, S. Xiong, *et al.*, "Dual-comb spectroscopy resolved three-degree-of-freedom sensing," *Photon. Res.* **9**, 243 (2021).
12. B. Chen, W. Mao, Y. Lou, *et al.*, "Simultaneous measurement of the straightness error and its position using a modified Wollaston-prism-sensing homodyne interferometer," *Meas. Sci. Technol.* **31**, 085004 (2020).
13. C. Ahn, Y. Na, and J. Kim, "Dynamic absolute distance measurement with nanometer-precision and MHz acquisition rate using a frequency comb-based combined method," *Opt. Lasers Eng.* **162**, 107414 (2023).
14. Y.-L. Chen, Y. Shimizu, J. Tamada, *et al.*, "Laser autocollimation based on an optical frequency comb for absolute angular position measurement," *Precis. Eng.* **54**, 284 (2018).
15. X. Liang, J. Lin, T. Wu, *et al.*, "Absolute angular measurement with optical frequency comb using a dispersive interferometry," *Opt. Express* **28**, 36095 (2020).
16. J.-A. Kim, J. W. Kim, C.-S. Kang, *et al.*, "On-machine calibration of angular position and runout of a precision rotation stage using two absolute position sensors," *Measurement* **153**, 107399 (2020).
17. Y. Choe and C. G. Park, "LiDAR-inertial-based absolute positioning with sparse DEM for accurate lunar landing," *IEEE Trans. Aerospace Electron. Syst.* **60**, 3482 (2024).
18. R. Paris, M. Melik-Merkumians, and G. Schitter, "Probabilistic absolute position sensor based on objective laser speckles," *IEEE Trans. Instrum. Meas.* **65**, 1188 (2016).

19. X. Guo, Y. Ding, Y. Duan, *et al.*, "Nonreciprocal metasurface with space-time phase modulation," *Light Sci. Appl.* **8**, 123 (2019).
20. Y. Yin, Q. Jiang, H. Wang, *et al.*, "Color holographic display based on complex-amplitude metasurface," *Laser Photon. Rev.* **19**, 2400884 (2025).
21. N. A. Rubin, Z. Shi, and F. Capasso, "Polarization in diffractive optics and metasurfaces," *Adv. Opt. Photon.* **13**, 836 (2021).
22. H. Zang, Z. Xi, Z. Zhang, *et al.*, "Ultrasensitive and long-range transverse displacement metrology with polarization-encoded metasurface," *Sci. Adv.* **8**, eadd1973 (2022).
23. H. Zang, Z. Zhang, Z. Huang, *et al.*, "High-precision two-dimensional displacement metrology based on matrix metasurface," *Sci. Adv.* **10**, eadk2265 (2024).
24. R. Barboza, A. Babazadeh, L. Marrucci, *et al.*, "Ultra-sensitive measurement of transverse displacements with linear photonic gears," *Nat Commun* **13**, 1080 (2022).
25. A. Tittl, A. Leitis, M. Liu, *et al.*, "Imaging-based molecular barcoding with pixelated dielectric metasurfaces," *Science* **360**, 1105 (2018).
26. S. Wen, X. Xue, S. Wang, *et al.*, "Metasurface array for single-shot spectroscopic ellipsometry," *Light Sci. Appl.* **13**, 88 (2024).
27. S. Rao, Y. Huang, K. Cui, *et al.*, "Anti-spoofing face recognition using a metasurface-based snapshot hyperspectral image sensor," *Optica* **9**, 1253 (2022).
28. M. Song, L. Feng, P. Huo, *et al.*, "Versatile full-colour nanopainting enabled by a pixelated plasmonic metasurface," *Nat. Nanotechnol.* **18**, 71 (2023).